A Semi-spectral Primitive Equation Ocean Circulation Model Using Vertical Sigma and Orthogonal Curvilinear Horizontal Coordinates

DALE B. HAIDVOGEL

Chesapeake Bay Institute, The Johns Hopkins University, Baltimore, Maryland 21218

JOHN L. WILKIN

Department of Ocean Engineering, Woods Hole Oceanographic Institution, 98 Water Street, Falmouth, Massachusetts 02543

AND

ROBERTA YOUNG

Department of Earth, Atmospheric and Planetary Science, Massachusetts Institute of Technology, Cambridge, Massachusetts 02139

We describe a new diabatic primitive equation model for studying regional and basin-scale ocean circulation processes. The model features coordinate transformations that efficiently incorporate moderately irregular basin geometries and large variations in bottom topography, and permits the inclusion of both thermal and wind forcing. A novel semi-spectral solution procedure, in which the vertical structure of the model variables is represented as a finite sum of user-specifiable structure functions (e.g., Chebyshev polynomials), provides faster-than-algebraic convergence of the vertical approximation scheme. Model performance is assessed on a variety of test problems drawn from coastal and large-scale oceanography including unforced, linear wave propagation in both regular and irregular geometries; non-linear flow over rough bottom topography; and eddy/mean flow interaction in a wind-driven, mid-latitude ocean basin. Computational efficiency of the model is found to be comparable to other existing primitive equation ocean models despite the utilization of the higher order spectral methods. © 1991 Academic Press, Inc.

1. INTRODUCTION

It is now widely recognized that numerical ocean models are powerful tools for studying oceanic circulation processes. For example, in large-scale dynamical oceanography, eddy-resolving, wind-driven, and thermodynamically active numerical models have led to improved understanding of the gyre-scale and global ocean

151

circulation, and to preliminary efforts at regional data assimilation and prediction [13]. Similarly, in coastal oceanography, studies of many aspects of coastal-trapped wave propagation, upwelling, and mean-flow generation [6] have necessitated the formulation of models able to accommodate stratification and the irregular geometry of a coastal ocean, and to realistically parameterize the processes of wind-driving and bottom friction. For a sampler of the wide variety of numerical models presently in use in oceanography, we refer the reader to the model descriptions collected in [20, 29, 30]. Many of the studies described therein used models which, either by approximation to the governing equations or geometric simplification, are applicable only to a particular class of problems or geographic location. Other studies where conducted with models having sufficient generality to allow their application to a wide variety of oceanographic problems.

For a regional or basin-scale numerical ocean model to be applicable to a broad class of process-oriented studies, it is desirable that it include as many of the following features as possible: the accommodation of spatially and temporally varying wind and thermal forcing; the effects of steep and/or tall topographic features; an appropriate parameterization of subgridscale dissipative, and surface and bottom frictional processes; flexibility in the specification of open boundary conditions; and accurate and efficiently implemented solution algorithms. Several classes of regional ocean models presently exist which incorporate some or all of the above features. The dynamically most simple, but computationally most efficient, of these are the quasigeostrophic (QG) models which have been employed in many process-oriented and predictive studies of western boundary current dynamics, and the origin and role of oceanic mesoscale eddies (see, e.g., [22, 27, 34, 35]). In dynamically more complex problems—for example, in those characterized by strongly ageostrophic currents, strong thermal forcing, and/or steep topography—it has been customary to rely on the primitive equations (PE) of oceanic motion; such PE models are in general use in global, basin-scale, and coastal ocean modeling (see, e.g., [4, 11, 16, 36]). Lastly, models intermediate in dynamical complexity and computational expense between the QG and PE models are beginning to offer an alternative for regional and large-scale modeling [2, 26].

Here, we introduce a semi-spectral primitive equation model (SPEM) which incorporates the features listed above. The model is thus applicable to studies of a wide range of oceanic processes and phenomena as demonstrated by the test problems and model applications described in the following sections. The principal technical advance incorporated into the SPEM is the implementation of a spectral method whereby the vertical structure of all the model variables is represented as an expansion in a finite set of continuous basis functions. This method offers several advantages in terms of efficiency and accuracy over traditional low-order finite-difference schemes.

The vertical spectral method is not new to oceanography, having been employed previously in models of tidal- and wind-driven flows in shallow continental shelf seas and of QG oceanic flow, in which the choice of basis functions is generally made to satisfy certain natural boundary conditions [14, 20]. Here, an expansion

in terms of orthogonal polynomials gives a rate of convergence which is faster than any finite power of the number of basis functions, and is dependent only upon the smoothness of the solution, and not on the speciality of the boundary conditions [32].

The paper is organized as follows. The primitive equations of motion, and the coordinate transformations adopted in the model, are outlined in Section 2. Section 3 presents the numerical algorithms employed by the model, including detailed descriptions of the spectral method, and the variance-conserving differencing scheme. Model performance is assessed in Sections 4 through 7 by reference to a sequence of analytic and semi-analytic test problems, and intercomparisons with results from other regional ocean models. Lastly, Section 8 discusses the model performance, with particular reference to the efficiency of computation on modern vector-processing computers.

2. MODEL FORMULATION

2a. *Equations of Motion*

As is traditional in diabatic, large- and regional-scale ocean circulation modeling (see, for example, [11]), we adopt the hydrostatic primitive equations, which can be written

$$\frac{\partial u}{\partial t} + \mathbf{v} \cdot \nabla u - fv = -\frac{\partial}{\partial x} \phi + \mathscr{F}_u + D_u \tag{2.1}$$

$$\frac{\partial v}{\partial t} + \mathbf{v} \cdot \nabla v + fu = -\frac{\partial}{\partial y} \phi + \mathscr{F}_v + D_v \tag{2.2}$$

$$\frac{\partial \phi}{\partial z} = \frac{-\rho g}{\rho_0} \tag{2.3}$$

$$\frac{\partial \rho}{\partial t} + \mathbf{v} \cdot \nabla \rho = \mathscr{F}_\rho + D_\rho \tag{2.4}$$

and

$$\frac{\partial u}{\partial x} + \frac{\partial v}{\partial y} + \frac{\partial w}{\partial z} = 0, \tag{2.5}$$

where, in standard notation:

$$(u, v, w) = (x, y, z) \text{ components of vector velocity } \mathbf{v}$$

$$\rho_0 + \rho(x, y, z, t) = \text{total density}$$

$$\phi = \text{dynamic pressure } (p/\rho_0)$$

$$f = \text{Coriolis parameter}$$

and

$$g = \text{acceleration of gravity.}$$

Equations (2.1) and (2.2) express the momentum balance in the x and y directions, respectively. In the Boussinesq approximation, density variations are neglected in the momentum equations except in their contribution to the buoyancy force in the vertical momentum equation (2.3). Under the hydrostatic approximation, it is further assumed that the vertical pressure gradient balances the buoyancy force. The time evolution of the density field, $\rho(x, y, z, t)$ is governed by the advective–diffusive equation (2.4). Lastly, Eq. (2.5) expresses continuity for an incompressible fluid. For the moment, the effects of forcing and dissipation will be represented by the schematic terms $\mathscr{F}$ and D, respectively. Formulations of the dissipation terms D presently in use in oceanographic modeling include smoothing based on harmonic and/or biharmonic operators, and Shapiro filters [16]. The separation of (2.4) into two independent prognostic equations for temperature and salinity and an equation of state is straightforward, but will not be discussed here.

2b. *Sigma (Stretched Vertical) Coordinate System*

It is computationally convenient to introduce a stretched vertical coordinate system which conforms to the variable bottom at $z = -h(x, y)$. Such "sigma" coordinate systems have long been used in both meteorology and oceanography (e.g., [33, 15]). To proceed, we make the coordinate transformation:

$$\hat{x} = x$$

$$\hat{y} = y$$

$$\sigma = 1 + 2(z/h)$$

and

$$t = t.$$

In the stretched system, the vertical coordinate σ spans the range $-1 \leqslant \sigma \leqslant 1$; we are therefore left with level upper ($\sigma = 1$) and lower ($\sigma = -1$) bounding surfaces. As a trade-off for this geometric simplification, the dynamic equations become somewhat more complicated. The resulting dynamic equations are, after dropping the carats,

$$\frac{\partial u}{\partial t} - fv + \mathbf{v} \cdot \nabla u = -\frac{\partial \phi}{\partial x} + (1 - \sigma)\left(\frac{g\rho}{2\rho_0}\right)\frac{\partial h}{\partial x} + \mathscr{F}_u + D_u \qquad (2.6)$$

$$\frac{\partial v}{\partial t} + fu + \mathbf{v} \cdot \nabla v = -\frac{\partial \phi}{\partial y} + (1 - \sigma)\left(\frac{g\rho}{2\rho_0}\right)\frac{\partial h}{\partial y} + \mathscr{F}_v + D_v \qquad (2.7)$$

$$\frac{\partial \phi}{\partial \sigma} = \left(\frac{-gh\rho}{2\rho_0}\right) \qquad (2.8)$$

$$\frac{\partial \rho}{\partial t} + \mathbf{v} \cdot \nabla \rho = \mathscr{F}_\rho + D_\rho \qquad (2.9)$$

and

$$\frac{\partial}{\partial x}(hu) + \frac{\partial}{\partial y}(hv) + h\frac{\partial \Omega}{\partial \sigma} = 0, \qquad (2.10)$$

where

$$\mathbf{v} = (u, v, \Omega),$$

$$\mathbf{v} \cdot \nabla = u\frac{\partial}{\partial x} + v\frac{\partial}{\partial y} + \Omega\frac{\partial}{\partial \sigma},$$

and the vertical velocity in sigma coordinates:

$$\Omega(x, y, \sigma, t) = \frac{1}{h}\left[(1-\sigma)u\frac{\partial h}{\partial x} + (1-\sigma)v\frac{\partial h}{\partial y} + 2w\right].$$

2c. Curvilinear Horizontal Coordinates

In many applications of interest (e.g., flow adjacent to a coastal boundary), the fluid may be confined horizontally within an irregular region. In such problems, a horizontal coordinate system which conforms to the irregular lateral boundaries is advantageous. Additionally, in many geophysical problems, the simulated flow field may have regions of enhanced structure (e.g., boundary currents or fronts) which occupy a relatively small fraction of the physical domain. In such problems, added efficiency can be gained by placing more computational resolution in these regions.

The requirement for a boundary-following coordinate system which allows laterally variable grid resolution can be met (for suitably smooth domains) by introducing an appropriate orthogonal coordinate transformation in the horizontal. Let the new coordinates be $\xi(x, y)$ and $\eta(x, y)$, where the relationship of horizontal arc length to the differential distances is given by:

$$(ds)_\xi = \left(\frac{1}{m}\right)d\xi \qquad (2.11a)$$

and

$$(ds)_\eta = \left(\frac{1}{n}\right)d\eta. \qquad (2.11b)$$

Here, $m(\xi, \eta)$ and $n(\xi, \eta)$ are the metric factors of the coordinate transformation which relate the differential distances $(\Delta\xi, \Delta\eta)$ to the actual (physical) arc lengths.

Denoting the velocity components in the new coordinate system by

$$\mathbf{v} \cdot \hat{\xi} = u \qquad (2.12a)$$

and

$$\mathbf{v} \cdot \hat{\eta} = v, \qquad (2.12b)$$

the equations of motion [(2.6)–(2.10)] can be re-written [3]:

$$\frac{\partial}{\partial t}\left(\frac{hu}{mn}\right) + \frac{\partial}{\partial \xi}\left(\frac{hu^2}{n}\right) + \frac{\partial}{\partial \eta}\left(\frac{huv}{m}\right) + \frac{\partial}{\partial \sigma}\left(\frac{hu\Omega}{mn}\right)$$

$$-\left\{\left(\frac{f}{mn}\right) + v\frac{\partial}{\partial \xi}\left(\frac{1}{n}\right) - u\frac{\partial}{\partial \eta}\left(\frac{1}{m}\right)\right\} hv$$

$$= -\left(\frac{h}{n}\right)\frac{\partial \phi}{\partial \xi} + (1-\sigma)\left(\frac{gh\rho}{2\rho_0 n}\right)\frac{\partial h}{\partial \xi} + \mathscr{F}_u + D_u \tag{2.13}$$

$$\frac{\partial}{\partial t}\left(\frac{hv}{mn}\right) + \frac{\partial}{\partial \xi}\left(\frac{huv}{n}\right) + \frac{\partial}{\partial \eta}\left(\frac{hv^2}{m}\right) + \frac{\partial}{\partial \sigma}\left(\frac{hv\Omega}{mn}\right)$$

$$+\left\{\left(\frac{f}{mn}\right) + v\frac{\partial}{\partial \xi}\left(\frac{1}{n}\right) - u\frac{\partial}{\partial \eta}\left(\frac{1}{m}\right)\right\} hu$$

$$= -\left(\frac{h}{m}\right)\frac{\partial \phi}{\partial \eta} + (1-\sigma)\left(\frac{gh\rho}{2\rho_0 m}\right)\frac{\partial h}{\partial \eta} + \mathscr{F}_v + D_v \tag{2.14}$$

$$\frac{\partial \phi}{\partial \sigma} = -\left(\frac{gh\rho}{2\rho_0}\right) \tag{2.15}$$

$$\frac{\partial}{\partial t}\left(\frac{h\rho}{mn}\right) + \frac{\partial}{\partial \xi}\left(\frac{hu\rho}{n}\right) + \frac{\partial}{\partial \eta}\left(\frac{hv\rho}{m}\right) + \frac{\partial}{\partial \sigma}\left(\frac{h\Omega\rho}{mn}\right) = \mathscr{F}_\rho + D_\rho \tag{2.16}$$

and

$$\frac{\partial}{\partial \xi}\left(\frac{hu}{n}\right) + \frac{\partial}{\partial \eta}\left(\frac{hv}{m}\right) + \frac{\partial}{\partial \sigma}\left(\frac{h\Omega}{mn}\right) = 0. \tag{2.17}$$

2d. Boundary and Initial Conditions

Consider a fluid lying within the three-dimensional domain $0 \leqslant \xi \leqslant L_x$, $0 \leqslant \eta \leqslant L_y$, and $-1 \leqslant \sigma \leqslant +1$, the latter corresponding to the depth range $0 \leqslant z \leqslant -h(x, y)$. Then, given an appropriate set of boundary and initial conditions, Eqs. (2.13)–(2.17) can, in principle, be solved for the time evolution of the fluid motion. In all the test problems described below, the upper and lower bounding surfaces are taken to be rigid; hence,

$$(\Omega)_{\sigma = \pm 1} = 0. \tag{2.18}$$

Applying the so-called "rigid-lid" surface boundary condition eliminates from the solution high speed surface gravity waves which would otherwise severely constrain the model timestep. The lateral boundaries at $\eta = 0$, L_y will likewise be impermeable:

$$(v)_{\eta = 0, L_y} = 0. \tag{2.19}$$

Finally, the remaining lateral boundaries ($\xi = 0$, L_x) will be treated in one of three ways—either as periodic

$$(u, v, \Omega, \rho, \phi)_{\xi = 0} = (u, v, \Omega, \rho, \phi)_{\xi = L_x}, \tag{2.20}$$

as closed

$$(u)_{\xi = 0, L_x} = 0, \tag{2.21}$$

or as open. In the latter case, an Orlanski radiation condition [31, 10] is used, as described below.

3. NUMERICAL SOLUTION TECHNIQUES

3a. *Vertical Spectral Method*

The vertical (σ) dependence of the model variables is represented as an expansion in a finite polynomial basis set $P_k(\sigma)$; that is, we set

$$b(\xi, \eta, \sigma) = \sum_{k=0}^{N} P_k(\sigma) \, \hat{b}_k(\xi, \eta), \tag{3.1}$$

where the arbitrary variable b, introduced here for the purposes of discussion, is any of u, v, ρ, ϕ, or Ω. The only restriction placed on the form of the basis polynomials is that $\frac{1}{2} \int_{-1}^{1} P_k(\sigma) \, d\sigma = \delta_{0k}$, where δ_{0k} is the Kronecker delta—i.e., that only the lowest order polynomial ($k = 0$) may have a non-zero vertical integral. This isolates the external mode (or depth averaged component of the field) in the amplitude of the $k = 0$ polynomial. In practice, the spectral technique does not explicitly solve for the polynomial coefficients $\hat{b}_k$ but rather for the actual variable values at "collocation" points (or equivalent grid points) σ_n chosen to correspond to the location of the extrema of the highest order polynomial. The collocation point values b_n are thus defined as

$$b_n = b(\sigma_n) = \sum_{k=0}^{N} P_k(\sigma_n) \hat{b}_k, \qquad 0 \leqslant n \leqslant N, \tag{3.2}$$

and will be functions of (ξ, η). The polynomial coefficients $\hat{b}_k$ can be recovered from the collocation point values b_n by a linear matrix transformation. Consider a matrix F whose elements are

$$F_{nk} = P_k(\sigma_n) \tag{3.3}$$

and let b and $\hat{b}$ be column vectors whose elements are b_n and $\hat{b}_k$, respectively. Then

$$b = F\hat{b} \tag{3.4}$$

and, hence,

$$\hat{b} = F^{-1}b. \tag{3.5}$$

It is now straightforward to represent vertical differentiation and integration in terms of matrix operators. Consider a matrix R whose elements are

$$R_{nk} = \frac{\partial P_k}{\partial \sigma}(\sigma_n). \tag{3.6}$$

Then the matrix $C_{DZ} = RF^{-1}$ will perform differentiation of the model field (b) in the vertical direction, denoted in the following subsections by the δ_σ operation, since

$$\delta_\sigma b = \frac{\partial b}{\partial \sigma} = \sum_{k=0}^{N} \frac{\partial P_k}{\partial \sigma}(\sigma_n)\hat{b}_k = R\hat{b} = RF^{-1}b = C_{DZ}b. \tag{3.7}$$

Similarly, consider a matrix $\mathscr{S}$ whose elements are

$$\mathscr{S}_{nk} = \int_{\sigma_n}^{1} P_k(\sigma)\,d\sigma. \tag{3.8}$$

Then the matrix $C_{INT} = \mathscr{S}F^{-1}$ will perform vertical integration, denoted in the following sections by the I_σ^1 operation, since

$$I_\sigma^1 b = \int_0^1 b\,d\sigma = \sum_{k=0}^{N}\int_{\sigma_n}^1 P_k(\sigma)\,d\sigma\hat{b}_k = \mathscr{S}\hat{b} = \mathscr{S}F^{-1}b = C_{INT}b. \tag{3.9}$$

In the model simulations reported in Sections 4, 5, and 6, Chebyshev polynomials were employed as the basis functions. The matrix operators F, R, and $\mathscr{S}$ and collocation levels σ_n for this basis set are given in the Appendix. An illustration of the use of a more generalized polynomial basis set is given in Section 7.

3b. *Horizontal Grid System*

In the horizontal coordinates (ξ, η), a traditional, centered, second-order finite-difference approximation is adopted. In particular, the horizontal arrangement of
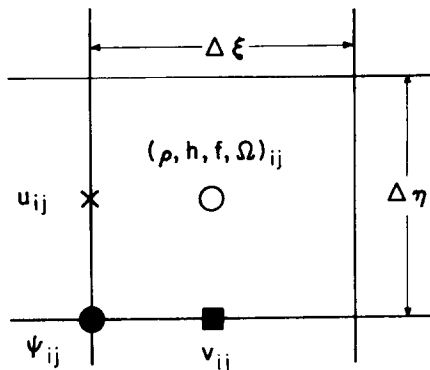

FIG. 1.   Schematic diagram showing the placement of variables on the Arakawa C grid.

variables is as shown in Fig. 1. This is equivalent to the well-known Arakawa "C" grid, which is well suited for problems with horizontal resolution that is fine compared to the first internal radius of deformation [3].

3c. *Semi-discrete Equations*

Using the representations described in Sections 3a and 3b, the semi-discrete form of the dynamic equations (2.13)–(2.17) becomes:

$$
\frac{\partial}{\partial t}\left(\overline{\left(\frac{h}{mn}\right)}^{\xi} u\right) + \delta_{\xi}\left\{\bar{u}^{\xi}\overline{\left(u\overline{\left(\frac{h}{n}\right)}^{\xi}\right)}^{\xi}\right\} + \delta_{\eta}\left\{\bar{u}^{\eta}\overline{\left(v\overline{\left(\frac{h}{m}\right)}^{\eta}\right)}^{\xi}\right\} + \delta_{\sigma}\left\{u\overline{\left(\frac{h\Omega}{mn}\right)}^{\xi}\right\}
$$

$$
-\left\{\overline{\left(\frac{fh}{mn}\right)}^{\xi\eta} + \bar{v}^{\xi}\bar{h}^{\xi\eta}\overline{\delta_{\xi}\left(\frac{1}{n}\right)}^{\xi\eta} - \bar{u}^{\eta}\bar{h}^{\xi\eta}\overline{\delta_{\eta}\left(\frac{1}{m}\right)}^{\xi\eta}\right\}^{\eta}\bar{v}^{\xi}
$$

$$
= -\overline{\left(\frac{h}{n}\right)}^{\xi}\delta_{\xi}\phi + (1-\sigma)\overline{\left(\frac{gh\rho}{2\rho_0 n}\right)}^{\xi}\delta_{\xi}h + \mathscr{F}_u + D_u \tag{3.10}
$$

$$
\frac{\partial}{\partial t}\left(\overline{\left(\frac{h}{mn}\right)}^{\eta} v\right) + \delta_{\xi}\left\{\bar{v}^{\xi}\overline{\left(u\overline{\left(\frac{h}{n}\right)}^{\xi}\right)}^{\eta}\right\} + \delta_{\eta}\left\{\bar{v}^{\eta}\overline{\left(v\overline{\left(\frac{h}{m}\right)}^{\eta}\right)}^{\eta}\right\} + \delta_{\sigma}\left\{v\overline{\left(\frac{h\Omega}{mn}\right)}^{\eta}\right\}
$$

$$
+\left\{\overline{\left(\frac{fh}{mn}\right)}^{\xi\eta} + \bar{v}^{\xi}\bar{h}^{\xi\eta}\overline{\delta_{\xi}\left(\frac{1}{n}\right)}^{\xi\eta} - \bar{u}^{\eta}\bar{h}^{\xi\eta}\overline{\delta_{\eta}\left(\frac{1}{m}\right)}^{\xi\eta}\right\}^{\xi}\bar{u}^{\eta}
$$

$$
= -\overline{\left(\frac{h}{m}\right)}^{\eta}\delta_{\eta}\phi + (1-\sigma)\overline{\left(\frac{gh\rho}{2\rho_0 m}\right)}^{\eta}\delta_{\eta}h + \mathscr{F}_v + D_v \tag{3.11}
$$

$$
\frac{\partial\phi}{\partial\sigma} = -\left(\frac{gh\rho}{2\rho_0}\right) \tag{3.12}
$$

$$
\frac{\partial}{\partial t}\left(\frac{h\rho}{mn}\right) + \delta_{\xi}\left\{u\overline{\left(\frac{h\rho}{n}\right)}^{\xi}\right\} + \delta_{\eta}\left\{v\overline{\left(\frac{h\rho}{m}\right)}^{\eta}\right\} + \delta_{\sigma}\left\{\frac{h\Omega\rho}{mn}\right\} = \mathscr{F}_\rho + D_\rho \tag{3.13}
$$

$$
\delta_{\xi}\left\{u\overline{\left(\frac{h}{n}\right)}^{\xi}\right\} + \delta_{\eta}\left\{v\overline{\left(\frac{h}{m}\right)}^{\eta}\right\} + \delta_{\sigma}\left\{\frac{h\Omega}{mn}\right\} = 0. \tag{3.14}
$$

Here δ_{ξ} and δ_{η} denote simple centered finite-difference approximations to $\partial/\partial\xi$ and $\partial/\partial\eta$, with the differences taken over the distances $\Delta\xi$ and $\Delta\eta$, respectively; $\overline{(\ )}^{\xi}$ and $\overline{(\ )}^{\eta}$ represent averages taken over the distances $\Delta\xi$ and $\Delta\eta$; δ_{σ} represents a vertical derivative evaluated according to the prescription given in 3a; and I_{σ}^1 indicates the analogous vertical integral.

3d. *Time-Stepping: Depth-Integrated Flow* $(k = 0$ *Mode*)

In their continuous form, the horizontal momentum and continuity equations (2.13), (2.14), and (2.17) can be written

$$\frac{\partial}{\partial t}\left(\frac{hu}{mn}\right) = R_u - \left(\frac{h}{n}\right)\frac{\partial \phi}{\partial \xi} \tag{3.15a}$$

$$\frac{\partial}{\partial t}\left(\frac{hv}{mn}\right) = R_v - \left(\frac{h}{m}\right)\frac{\partial \phi}{\partial \eta} \tag{3.15b}$$

and

$$\frac{\partial}{\partial \xi}\left(\frac{hu}{n}\right) + \frac{\partial}{\partial \eta}\left(\frac{hv}{m}\right) + \frac{\partial}{\partial \sigma}\left(\frac{h\Omega}{nm}\right) = 0, \tag{3.15c}$$

where R_u and R_v represent the sum of all other terms in the u and v equations, respectively. Performing a vertical average, the equations become

$$\frac{\partial}{\partial t}\left(\frac{h\bar{u}^\sigma}{mn}\right) = \bar{R}_u^\sigma - \left(\frac{h}{n}\right)\frac{\partial \bar{\phi}^\sigma}{\partial \xi} \tag{3.16a}$$

$$\frac{\partial}{\partial t}\left(\frac{h\bar{v}^\sigma}{mn}\right) = \bar{R}_v^\sigma - \left(\frac{h}{m}\right)\frac{\partial \bar{\phi}^\sigma}{\partial \eta} \tag{3.16b}$$

and

$$\frac{\partial}{\partial \xi}\left(\frac{h\bar{u}^\sigma}{n}\right) + \frac{\partial}{\partial \eta}\left(\frac{h\bar{v}^\sigma}{m}\right) = 0, \tag{3.16c}$$

where the overbar $(\bar{}^\sigma)$ indicates a vertically averaged quantity.

By virtue of the rigid-lid boundary condition (2.18), the depth-averaged flow is horizontally non-divergent. This enables us to introduce a streamfunction, $\psi(\xi, \eta, t)$, such that

$$\bar{u}^\sigma = -\left(\frac{n}{h}\right)\frac{\partial \psi}{\partial \eta} \tag{3.17a}$$

and

$$\bar{v}^\sigma = \left(\frac{m}{h}\right)\frac{\partial \psi}{\partial \xi}. \tag{3.17b}$$

By re-arrangement of (3.16a) and (3.16b)

$$\frac{\partial}{\partial t}\left(\frac{\bar{u}^\sigma}{m}\right) = \left(\frac{n}{h}\right)\bar{R}_u^\sigma - \frac{\partial \bar{\phi}^\sigma}{\partial \xi}$$

and

$$\frac{\partial}{\partial t}\left(\frac{\bar{v}^\sigma}{n}\right) = \left(\frac{m}{h}\right)\bar{R}_v^\sigma - \frac{\partial \bar{\phi}^\sigma}{\partial \eta}.$$

Finally, taking the curl of these equations yields a vorticity equation for the depth-averaged flow,

$$\frac{\partial}{\partial t} q = \frac{\partial}{\partial t}\left\{\frac{\partial}{\partial \xi}\left(\frac{\bar{v}^\sigma}{n}\right) - \frac{\partial}{\partial \eta}\left(\frac{\bar{u}^\sigma}{m}\right)\right\} = \frac{\partial}{\partial \xi}\left[\frac{m}{h}\,\bar{R}^\sigma_v\right] - \frac{\partial}{\partial \eta}\left[\frac{n}{h}\,\bar{R}^\sigma_u\right] \equiv R_q \qquad (3.18a)$$

or, using (3.17),

$$\frac{\partial}{\partial t}\left\{\left(\frac{m}{hn}\right)\frac{\partial^2 \psi}{\partial \xi^2} + \left(\frac{n}{hm}\right)\frac{\partial^2 \psi}{\partial \eta^2} + \frac{\partial}{\partial \xi}\left(\frac{m}{hn}\right)\frac{\partial \psi}{\partial \xi} + \frac{\partial}{\partial \eta}\left(\frac{n}{hm}\right)\frac{\partial \psi}{\partial \eta}\right\} = R_q. \qquad (3.18b)$$

The introduction of the streamfunction ψ serves two purposes. First, it automatically guarantees horizontal non-divergence, as required by (3.16c). Second, it eliminates any dependence on the depth-averaged component of the pressure field ϕ which contains an unknown contribution arising due to the rigid lid.

The vorticity equation (3.18b) is solved by first obtaining an updated value of q by application of the leapfrog (second-order) time-differencing scheme [19]. The associated value of the streamfunction is determined from the generalized elliptic equation:

$$\left(\frac{m}{hn}\right)\frac{\partial^2 \psi}{\partial \xi^2} + \left(\frac{n}{hm}\right)\frac{\partial^2 \psi}{\partial \eta^2} + \frac{\partial}{\partial \xi}\left(\frac{m}{hn}\right)\frac{\partial \psi}{\partial \xi} + \frac{\partial}{\partial \eta}\left(\frac{n}{hm}\right)\frac{\partial \psi}{\partial \eta} = q. \qquad (3.19)$$

A solution to (3.19) is fully prescribed by specifying values for ψ on the channel walls (in the case of a periodic channel), or on all four lateral boundaries (in the case of a closed domain). In the model test problems described below, Eq. (3.19) was solved using the elliptic equation solvers HWSCRT and MUD2 developed at the National Center for Atmospheric Research (NCAR).

3e. *Time-Stepping: Internal Velocity Modes and Density Field*

The N internal modes of the velocity distribution $((u, v)_k$ for $1 \leqslant k \leqslant N)$ are obtained by direct time-stepping of Eq. (3.10) and (3.11), having removed their depth-averaged component. The total density equation (3.13) can be similarly advanced for all $0 \leqslant k \leqslant N$. A leapfrog step is used in both cases. (A periodic application of an Euler or leapfrog–trapezoidal time step is used to diminish the computational mode.)

3f. *Determination of the Vertical Velocity and Pressure Fields*

Having obtained a complete specification of the u, v, and ρ fields at the next time level by the methods outlined above, the vertical velocity and internal pressure fields can be obtained by vertical integration; in particular,

$$\phi(\sigma) = \left(\frac{gh}{2\rho_0}\right) I^1_\sigma \rho \qquad (3.20)$$

and

$$\Omega(\sigma) = \left(\frac{mn}{h}\right) I_\sigma^1 \left\{\delta_\xi \left[\overline{u\left(\frac{h}{m}\right)}^\xi\right] + \delta_\eta \left[\overline{v\left(\frac{h}{m}\right)}^\eta\right]\right\}. \tag{3.21}$$

3g. Conservation Properties

It is traditional to require numerical models of the ocean and atmosphere to preserve the low-order conservation properties of the continuous equations of motion on which they are based. It is important to note, therefore, that the mixed spectral/finite difference solution procedure described above can be generalized to permit exact (within time-stepping error) conservation of such physical quantities as total momentum and energy.

For example, it can be easily shown that the inviscid ($D = 0$), unforced ($\mathscr{F} = 0$), discrete equations of motion (3.10)–(3.14) properly conserve the total (volumed integrated) values of momentum (u and v) and density (ρ) within closed or periodic domains. (Within an open domain, the gain/loss of total momentum or density can be precisely related to boundary fluxes of the two respective quantities.) The advective conservation of total u, v, and ρ (the "first moments") is guaranteed in this case because the discrete estimates of horizontal and vertical advection in Eqs. (3.10), (3.11), and (3.13) independently sum out when integrated over the horizontal ($0 \leqslant \xi \leqslant L_x$, $0 \leqslant \eta \leqslant L_y$) and vertical ($-1 \leqslant \sigma \leqslant +1$) extent of the computational domain for either periodic or closed geometries.

As in the case of three-dimensional, finite-difference models [3], however, conservation of additional, higher order invariants requires special treatment of the advective terms. Of course, the specifics of the treatment will necessarily depend on the higher order quantity being conserved. Suppose, for example, we wish to guarantee advective conservation of the second moments of u, v, and ρ (corresponding to kinetic energy (u^2, v^2) and density variance (ρ^2)). In analogy to (2.13), (2.14), and (2.16), we write the general form of the equation of motion as

$$\frac{\partial}{\partial t}\left(\frac{hQ}{mn}\right) + \frac{\partial}{\partial \xi}\left(\frac{huQ}{n}\right) + \frac{\partial}{\partial \eta}\left(\frac{hvQ}{m}\right) + A_Q = R_Q, \tag{3.22}$$

where Q represents either u, v, or ρ; R_Q stands for other terms in the Q equation; and A_Q is the desired conservative estimate for the vertical advective term.

From (3.22), a corresponding equation for the conservation of Q^2 can be derived by: first, applying the continuity equation (2.17); second, multiplying by $2Q$; and once again utilizing (2.17). The result is

$$\frac{\partial}{\partial t}\left(\frac{hQ^2}{mn}\right) + \frac{\partial}{\partial \xi}\left(\frac{huQ^2}{n}\right) + \frac{\partial}{\partial \eta}\left(\frac{hvQ^2}{m}\right) + \left[2QA_Q - Q^2\frac{\partial}{\partial \sigma}\left(\frac{h\Omega}{mn}\right)\right] = 2QR_Q. \tag{3.23}$$

The simultaneous requirements that both total Q and Q^2 be conserved are therefore met if

$$\int dv(A_Q) = 0 \tag{3.24a}$$

and if

$$\int dv(2QA_Q) = \int dv \left[Q^2 \frac{\partial}{\partial \sigma} \left(\frac{h\Omega}{mn} \right) \right], \tag{3.24b}$$

where $\int dv$ signifies a volume integral.

For simpler finite-difference models, the analogous constraints can simultaneously be met by simple averaging of Q in the estimate of the vertical advection term [25]. Here, the situation is complicated by the spectral formalism being used in the σ coordinate. Conservative algorithms can, nonetheless, be constructed. The simplest approach we have found is to set

$$A_Q = \delta_\sigma \left(\frac{h\Omega Q}{mn} \right) + \alpha(Q - \bar{Q}^\sigma) \tag{3.25a}$$

with

$$\alpha = \frac{\int dv \left[Q^2 \frac{\partial}{\partial \sigma} \left(\frac{h\Omega}{mn} \right) - 2Q \frac{\partial}{\partial \sigma} \left(\frac{h\Omega Q}{mn} \right) \right]}{\int dv [2Q(Q - \bar{Q}^\sigma)]}. \tag{3.25b}$$

Use of the vertical advection estimate (3.25a) and (3.25b) formally guarantees first and second moment conservation of the advected quantity Q. It has been used, for example, to guarantee variance conservation in a multi-year simulation of the turbulent, wind-driven ocean circulation (Section 7).

4. MODEL PERFORMANCE: FREE WAVES IN A STRAIGHT COASTAL CHANNEL

A variety of test problems has been studied to determine the accuracy and computational character of the model as a function of both physical and numerical parameters. The tests included: (i) unforced, linear wave propagation in both regular and irregular geometries; (ii) simulations of non-linear flow over rough bottom topography, for which solutions from an independent numerical model were available; and (iii) an idealized simulation of the eddying, wind-driven mid-latitude ocean circulation. In (i) three classes of freely propagating subinertial-frequency linear waves were studied: barotropic shelf waves, baroclinic Kelvin waves, and coastal-trapped waves. Test (ii) examined non-linear wave/mean flow interaction, and the generation of topographic-stress-driven mean currents, while test (iii) considered the effects of such processes as barotropic and baroclinic instability.

Neglecting the effects of stratification, the presence of the sloping bottom of a continental shelf provides a potential vorticity gradient which supports an infinite set of waves termed barotropic shelf waves (BSWs). Alternatively, in a stratified ocean without coastal topography, there exists a set of waves termed baroclinic Kelvin waves (BKWs); these are essentially internal gravity waves modified by the

Earth's rotation. In a typical coastal ocean, both stratification and topography are present. As a result, observed subintertial-frequency waves are actually a hybrid class of waves, coastal-trapped waves (CTWs), having characteristics of both BSWs and BKWs. In actuality, BSWs and BKWs are not distinct sets of waves, but rather the low and high stratification limits, respectively, of CTWs.

The equations governing the propagation of these linear, inviscid waves written in Cartesian coordinates are

$$\frac{\partial u}{\partial t} - f_0 v = -\frac{\partial \phi}{\partial x} \tag{4.1}$$

$$\frac{\partial v}{\partial t} + f_0 u = -\frac{\partial \phi}{\partial y} \tag{4.2}$$

$$\frac{\partial \phi}{\partial z} = \frac{-g\rho'}{\rho_0} \equiv b \tag{4.3}$$

$$\frac{\partial b}{\partial t} + N^2 w = 0 \tag{4.4}$$

and

$$\frac{\partial u}{\partial x} + \frac{\partial v}{\partial y} + \frac{\partial u}{\partial z} = 0, \tag{4.5}$$

where the square of the buoyancy frequency

$$N^2(z) = \frac{-g}{\rho_0} \frac{\partial \bar{\rho}}{\partial z} \tag{4.6}$$

corresponds to some fixed background stratification $\bar{\rho}(z)$ defined such that the total density is

$$\rho = \rho_0 + \bar{\rho}(z) + \rho'(x, y, z, t) \tag{4.7}$$

and

$$\rho_0 \gg \bar{\rho} \gg \rho'. \tag{4.8}$$

An f-plane has been assumed.

Taking the coordinates x and y to be oriented alongshelf and across-shelf, respectively, and assuming that the coast is straight and the depth varies in y only, travelling wave solutions proportional to $\exp[i(lx - \omega t)]$ can be found, where l is the alongshelf wavenumber and ω is the frequency. Substitution of the traveling wave form into Eq. (4.1) through (4.5) yields the following expression for the across-shelf modal structure of the pressure perturbation of a free CTW:

$$\frac{\partial^2 \hat{\phi}}{\partial y^2} + (f_0^2 - \omega^2) \frac{\partial}{\partial z} \left(\frac{1}{N^2} \frac{\partial \hat{\phi}}{\partial z} \right) - l^2 \hat{\phi} = 0. \tag{4.9}$$

The boundary conditions on (4.9) are that there be no flow through the bottom $(\mathbf{v} \cdot \nabla h = 0$ at $z = -h)$ or through the channel walls $(v = 0$ at $y = 0$, $L_y)$. For a given $h(y)$, $N^2(z)$, f_0, and l, there is a sequence of solutions to (4.9) at discrete eigenfrequencies ω which are free CTWs [23].

In the following subsections, analytical and semi-analytical solutions to (4.9) corresponding to the particular cases of BSWs, BKWs, and CTWs are used to initialize the SPEM with periodic channel boundary conditions. The model is then advanced in time, and its performance gauged by computing the root-mean-square (RMS) departures of the computed velocity components (u, v) and buoyancy (b) from their analytical values at the end of one wave period.

4a. *Barotropic Shelf Waves*

While it is possible to solve (4.9) in the barotropic limit, $N^2 \to 0$ (e.g., [23]), it is more common to obtain BSW solutions by solving a vorticity equation, similar to (4.9), for the transport streamfunction ψ (e.g., see [9]). In particular, if the depth profile is assumed exponential

$$h(y) = e^{2\alpha y} \tag{4.10}$$

then the solution for ψ is

$$\psi(x, y, t) = \psi_0 e^{\alpha y} \sin(\gamma_m y) e^{i(lx - \omega t)}. \tag{4.11}$$

The boundary conditions require

$$\gamma_m = \frac{m\pi}{L_y}, \tag{4.12}$$

where L_y is the channel width, and m, an integer, is the mode number. The frequency of mode m is

$$\omega_m = \frac{2\alpha f_0 l}{l^2 + \gamma_m^2 + \alpha^2}. \tag{4.13}$$

As in Section 3, the streamfunction is related to the horizontal velocity components by the relations

$$(hu, hv) = \left(-\frac{\partial \psi}{\partial y}, \frac{\partial \psi}{\partial x} \right). \tag{4.14}$$

Having determined u and v, the remaining variables can be found using (4.1)–(4.5).

The SPEM, with non-linear and frictional terms removed, was initialized with the analytic solution (4.11). The wavenumber l was chosen such that the analytic solution satisfied the model's periodic boundary conditions, i.e., $l = (2\pi k/L_x)$, where k is an integer. The RMS errors in the computed solutions at the end of one wave period $(2\pi/\omega)$ are shown in Table I for several of the test problems. For fixed

domain size (L_x, L_y) and topographic e-folding scale (α), the accuracy of the numerical solution should depend on only three parameters:

$$N_x = \text{number of } x \text{ gridpoints per } x \text{ wavelength}$$
$$= \text{total number of } x \text{ gridpoints}/k$$
$$N_y = \text{number of } y \text{ gridpoints per cross-channel mode}$$
$$= \text{total number of } y \text{ grid points}/m$$

and

$$N_t = \text{number of time steps per wave period}$$
$$= (2\pi/\omega)/\Delta t.$$

In all tests, time-differencing errors are negligible ($N_t = 100$ or 200; see Table I), and the errors associated with horizontal differencing have been examined by systematically varying N_x and N_y. As expected for the second order, Arakawa C differencing scheme, Table I shows that the RMS errors display a crudely quadratic dependence on horizontal spatial resolution. Errors of about one percent after one wave period are obtained for $N_x = 40$ and $N_y = 20$.

4b. Baroclinic Kelvin Waves

If both h and N^2 are constant, then Eq. (4.9) is separable, and can be solved analytically for the modal structures of free BKWs:

$$\hat{\phi}(y, z) = \phi_0 e^{-f_0 y/c_m} G_m(z). \tag{4.15}$$

TABLE I

RMS Errors (in Percent) for the Horizontal Components
of Velocity (u, v) after One Wave Period
for Simulations of Barotropic Shelf Waves

k, j	N_x	N_y	N_t	$R(u)$	$R(v)$
1, 1	80	40	100	0.24	0.25
1, 2	80	20	100	0.48	0.49
2, 1	40	40	100	1.3	1.4
2, 2	40	20	100	1.2	1.2
4, 1	20	40	100	5.2	5.4
1, 4	80	10	100	4.2	4.3
4, 4	20	10	100	4.9	5.1
2, 2	24	20	200	1.0	1.1

Note. In all cases $(L_x, L_y, \alpha, f_0) = (100 \text{ km}, 40 \text{ km}, 4 \times 10^{-2} \text{ km}^{-1}, 10^{-4} \text{ s}^{-1})$.

Here, c_m is the phase speed of mode m:

$$c_m = \omega_m / l = \frac{Nh}{m\pi} \qquad (4.16)$$

and the vertical eigenfunctions are

$$G_m(z) = \begin{cases} 1, & m = 0 \\ \sqrt{2}\cos(m\pi z/H), & m > 0. \end{cases} \qquad (4.17)$$

As above, the other variables can be obtained from (4.1)–(4.5).

A sequence of initial value problems, analogous to that described in Section 4a, has been run to investigate the performance of the SPEM with respect to BKWs. For these cases, the relevant numerical parameters are:

N_x = number of x gridpoints per x wavelength

   = total number of x gridpoints$/k$

N_y = number of y gridpoints per off-shore e-folding scale

   = total number of y grid points$/(f_0 L_y/c_m)$

TABLE II

RMS Errors (in Percent) for Velocity (u, w) and Perturbation Buoyancy
(b) after One Wave Period for Simulations of Baroclinic Kelvin Waves

k, m	N_x	N_1	N_z	N_t	$R(u)$	$R(w)$	$R(b)$
1, 1	80	10	6	200	0.21	0.22	0.21
2, 1	40	10	6	200	0.69	0.74	0.71
4, 1	20	10	6	200	2.6	2.7	2.7
2, 1	40	5	12	200	0.68	0.71	0.69
2, 1	40	5	9	200	0.68	0.71	0.69
2, 1	40	5	6	200	0.68	0.72	0.69
2, 1	40	5	5	200	0.71	0.76	0.75
2, 1	40	5	4	200	1.3	1.5	1.6
2, 1	24	5	3	200	8.4	8.6	8.0
2, 2	40	2.5	12	200	0.80	1.3	0.86
2, 2	40	2.5	9	200	0.80	1.3	0.86
2, 2	40	2.5	6	200	0.80	1.3	0.86
2, 2	40	2.5	4	200	0.80	1.3	0.86
2, 2	40	2.5	3	200	1.4	2.3	2.2
2, 2	40	2.5	2.5	200	5.7	6.9	8.4
2, 2	40	2.5	2	200	32.2	34.7	32.3
2, 2	40	5	3	200	1.5	1.9	1.9
2, 1	40	10	6	400	0.66	0.71	0.67

Note. Except where noted, (L_x, L_y, f_0, N, H) = (200 km, 100 km, 10^{-4} s^{-1}, $20\pi f_0$, 1000 m). Errors are computed at the first interior level below the surface; errors at the other levels are comparable.

N_z = number of vertical degrees of freedom per vertical mode number

= number of Chebyshev polynomials/m

and

$$N_t = (2\pi/\omega)/\Delta t.$$

A representative set of BKW runs, and the associated RMS error levels, is summarized in Table II.

For the tests shown in Table II, time-differencing errors have again been kept small ($N_t = 200$ and 400). And, as above for the BSWs, a roughly quadratic dependence of errors on N_x and N_y is obtained. The interesting new feature of the BKW tests is that they exhibit non-trivial vertical structure (e.g., u and ϕ fields that vary in z as a cosine function). This gives some indication of the "resolving power" of the Chebyshev-collocation technique. In principle, the advantage of this technique (and other spectral approximation methods) is their faster-than-algebraic convergence rate. This dramatic property is demonstrated in Fig. 2, wherein the RMS errors in a simulation of the first- and second-mode BKWs are plotted as a function of N_z, for fixed horizontal and temporal resolution. Convergence to the limiting RMS error levels (corresponding to finite values of N_x, N_y, and N_t) is extremely rapid; for example, RMS errors are reduced from 32% to roughly 2% when the number of polynomials is increased by 50% from 4 ($N_z = 2$) to 6 ($N_z = 3$).
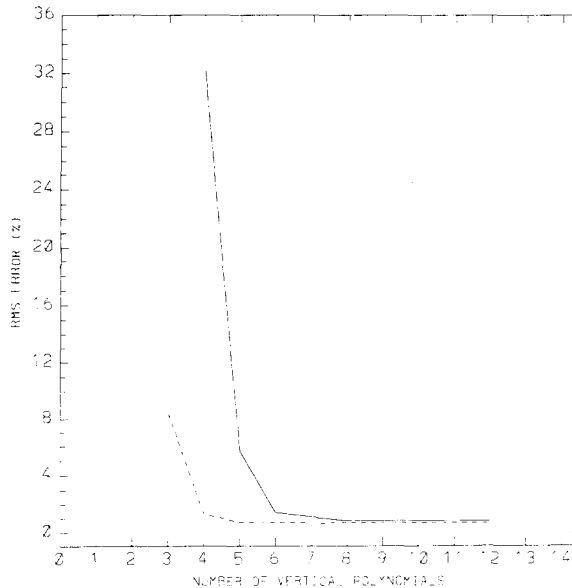
FIG. 2. RMS error (in percent) as a function of the number of vertical polynomials after one wave period in the simulation of baroclinic Kelvin waves. The mode 1 (dotted line) and mode 2 wave (solid line) are shown.

4c. Coastal-Trapped Waves

For arbitrarily varying h and N^2, Eq. (4.9) cannot be solved analytically. Solutions for $\hat{\phi}(y, z)$, and for the (ω, l) pairs corresponding to the free CTWs, must be determined numerically. In the model tests summarized below, $\hat{\phi}(y, z)$ and the modal structures of the other variables were computed with a numerical solution procedure developed specifically for use in conjunction with the SPEM. This solution procedure employs the same generalized horizontal and vertical coordinate systems, and the same discretization scheme (i.e., horizontal finite differences and a vertical expansion in Chebyshev polynomials) as the SPEM. Note that, in contrast to the previous examples, this initialization procedure uses a numerical approximation to the true solution.

As in Sections 4a and b, a sequence of simulations was conducted by initializing with a single CTW solution, and then advancing the model in time for one wave period. The topography chosen for the tests is typical of many continental shelves. It ranges in depth from 110 m at the coast to 4000 m in the abyssal ocean, 150 km from shore. The maximum slope (5.8×10^{-2}) occurs 100 km from shore at a depth of 2600 m. A linear stratification with constant N^2 value of $6.25 \times 10^{-6} s^{-2}$ was used. The strength of this stratification as estimated by the Burger number ($Nh_{max}/f_0 L_y$) is unity. An $O(1)$ value indicates that both topography and stratification play a significant role in the dynamics of the wave propagation.

TABLE III

RMS Errors (in Percent) for the Alongshelf (u) and
Across-shelf (v) Components of Velocity after One Wave Period
for Simulations of Coastal-Trapped Waves

Mode	N_x	N_y	N_z	N_t	$R(u)$	$R(v)$
1	80	100	6	300	0.48	0.52
1	40	100	6	300	1.31	1.43
1	20	100	6	300	7.10	8.02
1	80	200	6	600	0.31	0.33
1	40	50	6	300	1.79	1.96
1	40	100	12	300	1.32	1.44
1	40	100	3	300	1.51	2.23
2	60	100	6	600	1.65	2.11
2	40	100	6	600	2.30	2.79
2	40	150	6	900	1.80	2.16
3	40	100	6	900	4.23	28.4

Note. $L_x = 2\pi \times 10^2$ km, $L_y = 300$ km, $f_0 = 10^{-4}$ s^{-1}, and $N = 2.5 \times 10^{-3}$ s^{-1}. For all cases the wavenumber is $l = 10^{-5}$ m^{-1}. The wave frequency ω differs for each mode. For mode 1, $\omega = 5.1 \times 10^{-5}$ (period = 1.4 days); mode 2, $\omega = 2.5 \times 10^{-5}$ (2.9 days); mode 3, $\omega = 1.4 \times 10^{-5}$ (5.2 days). Errors are computed at the first interior level below the surface; errors at the other levels are comparable.

The RMS differences between the initial condition and the model solution after one wave period were calculated. These RMS errors are presented in Table III for various values of the parameters:

$$N_x = \text{number of } x \text{ gridpoints per } x \text{ wavelength}$$

$$N_y = \text{number of } y \text{ gridpoints across channel}$$

$$N_z = \text{number of Chebyshev polynomials}$$

$$N_t = \text{number of time steps per wave period.}$$

The vertical and across-shelf length scales of CTW modal structures are strongly dependent on details of the topography and stratification and are not a simple function of mode number; so, unlike the previous tests, N_y and N_z have not been adjusted by the CTW mode number.

Again, as in the tests of Sections 4a and b, a roughly quadratic dependence of the RMS errors on N_x is obtained. Errors decrease less rapidly with improved across-channel resolution. In the previous tests, the SPEM was compared with known analytical solutions. In these tests, the initial condition is only "semi-analytical," and it is probable that much of the adjustment between the "numerical waveform" and the true "analytical waveform" has already been effected in the numerical estimation of the across-shelf modal structures. Improved across-channel resolution is therefore less likely to yield substantial decreases in RMS error levels. The rate of convergence of the Chebyshev polynomial expansion to the limiting error levels is similar to that observed in the Kelvin wave tests. The error levels shown in Table III indicate that the model correctly propagates CTWs in a model environment where both bottom topographic variations and stratification are strong.

5. MODEL PERFORMANCE: FREE COASTAL-TRAPPED WAVES IN AN IRREGULAR COASTAL CHANNEL

An analytical solution for the scattering of a free BSW incident upon a discontinuity in shelf width in a coastal channel has been presented by Wilkin and

produces a strong alongshelf modulation in flow intensity downstream of the scattering region. By generating an orthogonal curvilinear coordinate grid fitted to a coastal channel whose width increases abruptly, it has been possible to use the SPEM to conduct a simulation of BSW scattering which duplicates almost exactly the problem considered by W&C.

The computer code used to generate the curvilinear grid [21] is based on an algorithm described by Ives and Zacharias [24] which first conformally maps the irregular channel boundary to a rectangle, and then fills in the grid by solving a

boundary-value elliptic problem. The grid geometry used in the simulation differs slightly from the problem considered by W&C in that, rather than being discontinuous, the channel width increases smoothly over a distance of 50 km. A step width change in the numerical grid would produce extremely small grid spacings in at least one region of the domain and place prohibitive constraints on the model time step. W&C suggest that their solution should not alter appreciably for width changes occurring over such a short alongshelf distance. The bottom depth has the same exponential profile introduced in Section 4a (W&C, Fig. 1). The incident wave is introduced into the computational domain by a numerical "wavemaker" which prescribes u, v, and ρ at each time-step at the open boundary at the narrow end of the channel. The across-shelf modal structures (u, v, and ρ) of the incident wave are computed using the same method described in Section 4c and the time dependence is simple harmonic.

The simulation begins with a quiescent channel and, to minimize initial transients, the wavemaker amplitude increases smoothly over two wave periods to a constant value. As the wave propagates through the width change, it scatters into a set of transmitted waves of different modes. An Orlanski radiation condition [31] combined with a Rayleigh damping sponge at the downstream open boundary allows the scattered waves to propagate out of the computational domain with minimal reflection. The amplitudes of the scattered modes are determined by performing a least-squares fit of the alongshelf velocity to a sum of the transmitted wave modal structures at an across-shelf section 200 km downstream of the scattering region and 400 km upstream from the beginning of the sponge. The least-squares-fit time series become periodic with constant amplitude shortly after the wavemake amplitude stops increasing. The amplitude of each time series is the amplitude of that scattered mode.

The particular case simulated is that of W&C's Table 1. The incident wave is mode 1, the frequency is $0.1f_0$, the shelf widths are 100 and 225 km and the topography has a decay scale $\alpha = 10^{-2}$ km^{-1}. The regular pattern of the mode 1 incident wave scatters into a more complicated pattern comprised of several scattered modes having different across-shelf structures and wavelengths. The least-
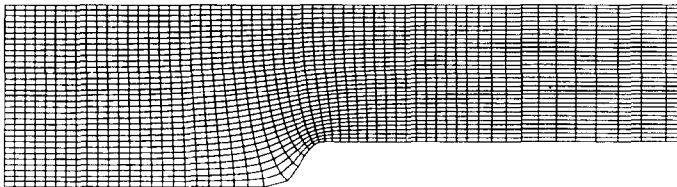

FIG. 3.   Horizontal orthogonal curvilinear coordinate grid used in the simulation of CTW scattering. For clarity, only every second grid line is plotted. Channel widths are 400 km at the left (upstream) and 300 km at the right. Note that the grid spacing increases toward the right (open) boundary. The total length shown is 1500 km. In the actual simulation, a further 500 km of stretched grid at the right end of the domain was included to accommodate the Rayleigh sponge layer.

squares fit gives amplitudes for the scattered modes 1, 2, and 3 of 0.360, 0.454, and 0.292, respectively, which compare favorably with the values 0.346, 0.461, and 0.316 calculated by W&C. The discrepancy is consistent with the smoother coastline change being less conductive to scattering into higher modes.

Several simulations similar to that described above have been conducted as part of a study of the scattering of CTWs by variations in topography and coastline in a stratified coastal ocean [40]. Results from one of these simulations are presented here as an illustration of the SPEM performance. The horizontal coordinate grid used in the example is shown in Fig. 3. For clarity, only half the grid lines are plotted. The channel decreases in width from 400 to 300 km over an alongshelf
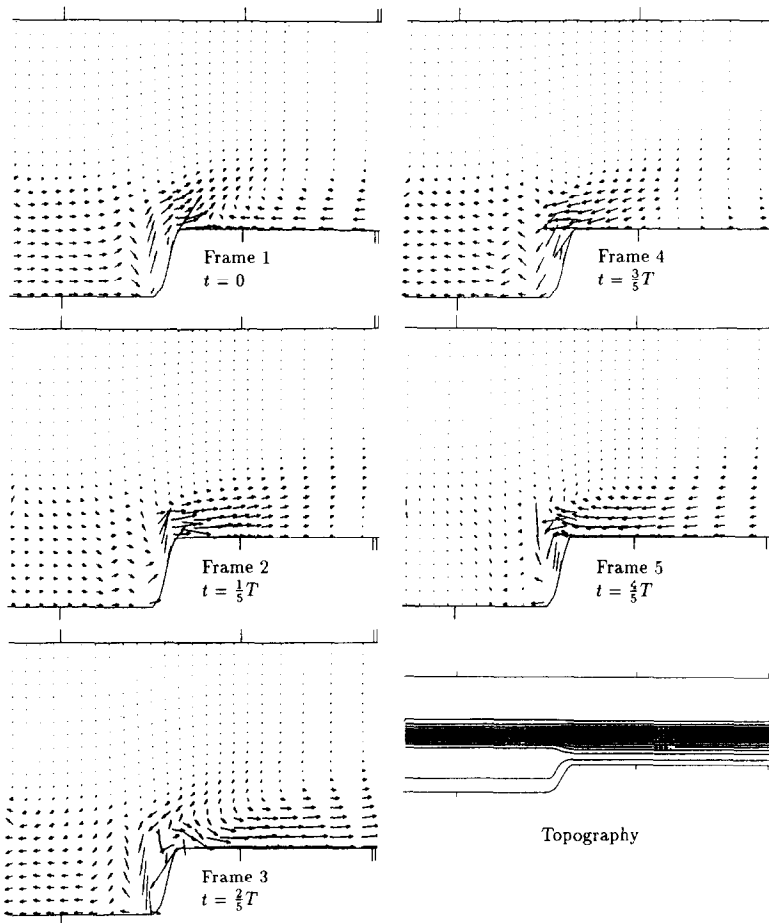
FIG. 4. A sequence of plots of surface velocity vectors at different times during a single wave period (T). The case shown is a mode 1 incident CTW with frequency 1×10^{-5} s^{-1}, approaching from the left, propagating through the topography shown in the lower right panel. Note that the across-shelf scale has been expanded for clarity.
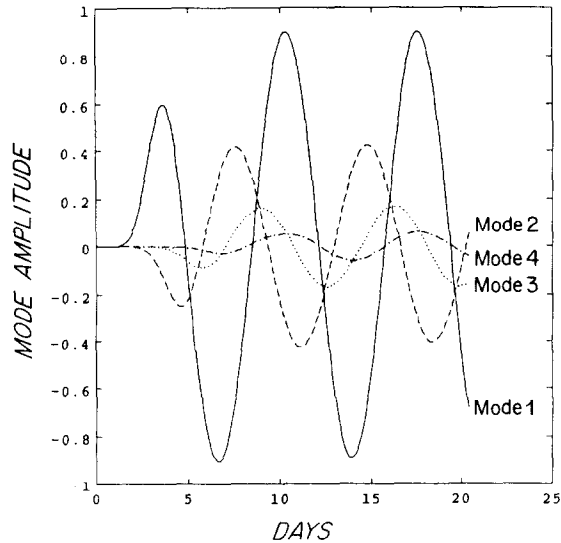
FIG. 5. Time series of CTW amplitudes obtained from a least squares fit to a sum of calculated CTW modal structures. The time series become periodic with constant amplitude shortly after the amplitude of the numerical wavemaker stops increasing. The higher modes, which propagate slower than the lower modes, take longer to reach constant amplitude.

distance of 100 km. Figure 4 shows surface velocity vectors at several different times during a single wave period for a mode 1 incident CTW approaching from the left. The bathymetry is shown in the lower right panel of the figure. There are regions within the area of changing topography where the wave-induced currents are amplified significantly, and where the directions of the currents vary considerably over short spatial scales.

Figure 5 shows the time series of the transmitted mode amplitudes calculated by least-squares fit at the location indicated by the single tick marks in Fig. 4. For the stratification and shelf topography used in this example, no CTWs can be generated which will propagate back toward the wave-maker. The energy flux in the transmitted modes should therefore balance the incident energy flux. Calculating energy fluxes from the least-squares fit amplitudes, it is found that the energy fluxes in the first three modes, normalized by the incident energy, are 0.821, 0.174, and 0.032, respectively. The energy in higher modes is negligible. The total transmitted energy flux computed by this method is therefore 1.032. The discrepancy in the energy level (3.2%) is attributable to uncertainties in the least-squares mode fit method.

6. MODEL PERFORMANCE: WIND-DRIVEN FLOW OVER IRREGULAR BOTTOM TOPOGRAPHY

Haidvogel and Brink ([17], hereafter, H&B) have described a sequence of numerical simulations of wind-driven flow over irregular continental shelf

topography. The objective of their study was to determine whether topographic stress, known to be asymmetric for barotropic flow over the shelf [5], can generate substantial time-averaged alongshelf currents in the presence of a fluctuating zero-mean wind stress. Their results, which were obtained with a barotropic, nonlinear model forced by a periodic spatially uniform alongshelf wind stress, and damped by linear bottom drag, demonstrate that topographic stress asymmetries can lead to observable mean currents on continental shelves. H&B's results present a partial explanation for certain observed mean currents that run counter to mean alongshore winds and indicate that this mechanism needs to be explored in greater detail, principally through the inclusion of stratification and improved parameterization of bottom friction.

To assess further the performance of the SPEM, a simulation has been conducted which duplicates the central experiment of H&B. The H&B model differs in several respects from ours; namely, it is purely barotropic, utilizes a non-staggered grid, and employs a Fourier (spectral) solution procedure in the x (periodic, alongshelf) direction. Establishing that the present model yields results nearly identical to the substantially different H&B model therefore serves to validate its performance in problems involving wind-forced, frictionally-damped, nonlinear flows.

The variable bottom topography for the central case of H&B is shown in Fig. 6. The coastal channel is 450 km in length, and 90 km in width. Monochromatic topographic "bumps" of wavelength 150 km are superimposed on a systematic offshore increase in depth. The fluid depth is 20 m at the coast ($y = 0$), and approximately 2000 m at the offshore boundary ($y = 90$ km). The midshelf depth perturbation associated with the bumps is approximately 40 m.

At $t = 0$, an alongshelf wind stress of 1 dyne/cm^2 is impulsively applied to the coastal channel. The wind stress is assumed to be perfectly oscillatory with a 10-day period. The fluid is allowed to adjust away from its (motionless) initial conditions
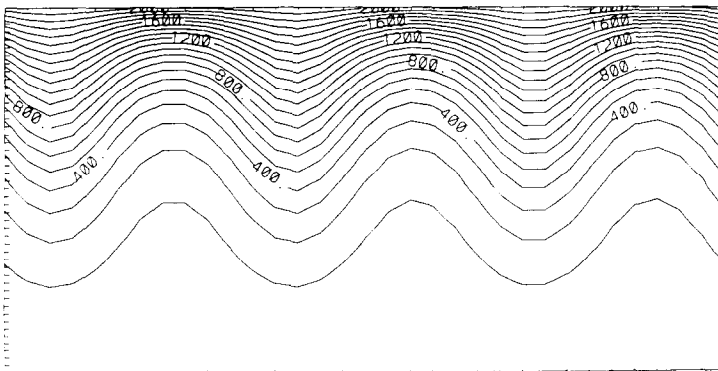

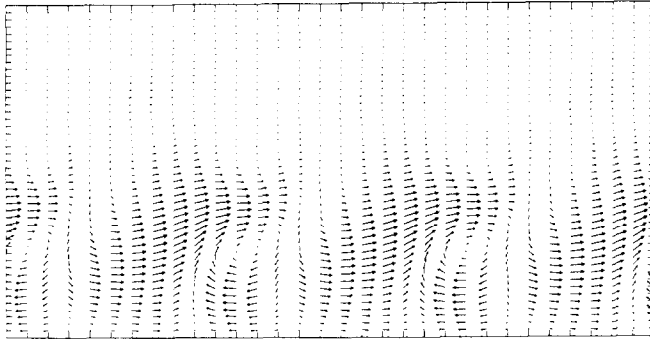FIG. 6. Variable topography used in the H&B simulation. Depth contours are given in meters.

FIG. 7. Time-mean Eulerian velocity vectors for the H&B simulation. The maximum vector length equals 1.45 cm s^{-1}.

Thereafter, a time-series ($260 < t \leqslant 300$ days) of the circulation in the channel is collected for analysis.

In order to duplicate the physical conditions of the H&B central experiment, the SPEM was modified to incorporate a depth-independent body force equal to the sum of the imposed wind stress and the retarding, linear bottom drag ($C_D = 3 \times 10^{-2}$ cm sec^{-1}). In addition, the alongshelf-acting biharmonic lateral friction term of H&B was added, although it plays little role in the time-averaged flow fields reported below. To mimic the homogeneous conditions of the H&B case, total density was set equal to the constant ρ_0. Lastly, all boundary conditions used were the analogues of those used by H&B. The model resolution used was (33×49) horizon-
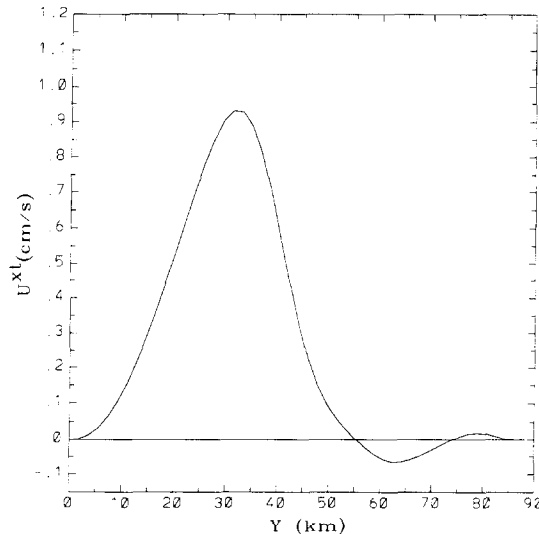
FIG. 8. Time and x-averaged residual current (u, in centimeters per second) as a function of offshore distance for the H&B simulation.

tal gridpoints, and $N = 2$ Chebyshev polynomials. (Since the fluid is homogeneous, and forced in a depth-independent manner, it is expected that the flow will at all times remain depth-independent. This was observed to be the case to machine accuracy.)

Figures 7 and 8 show the induced Eulerian circulation in the channel, obtained as a time-average over the last four forcing periods ($260 \leq t \leq 300$ days). These figures show the time-mean velocity vectors in the channel, and the time- and x-averaged residual current. Local maxima in the induced currents of approximately 1.45 cm sec^{-1} are generated by the presence of the topographic bumps by the associated topographic stress asymmetries. Averaged along-channel, the peak residual alongshore current is slightly less than 1 cm s^{-1}.

These figures may be directly compared to Fig. 5 and 6 of H&B. All qualitative features of the topographically induced mean circulation reported by H&B are reproduced by the SPEM. Good quantitative agreement is also achieved with the principal differences being a somewhat greater residual flow strength (about 10%), and a slightly broader induced prograde flow, in the SPEM results. These differences are primarily due to the sensitivity of the solution to changes in the horizontal grid scheme employed at fixed resolution.

7. AN EDDY-RESOLVING MODEL OF THE WIND-DRIVEN OCEAN CIRCULATION

A fundamental problem in the modeling of the oceanic general circulation is the adiabatic, statistical equilibrium response of a rectangular, mid-latitude ocean driven by steady surface wind stress. A variety of theoretical and numerical models have been applied to this problem in the past, beginning with the steady, frictional theories of Stommel [38] and Munk [28]. More recently, quasigeostrophic models have contributed to our understanding of the wind-driven response of a β-plane ocean, and to the associated equilibrium balance between eddies, turbulence, and the time-mean circulation (see, e.g., [34, 35]). Despite the successful application of QG models, however, other, more physically complete, model formulations—such as the primitive equations—have been much less extensively explored, particularly in the adiabatic limit.

In one such exploration, McWilliams *et al.* [26] relax two important restrictions of quasi-geostrophy: the β-plane form of the Coriolis force, and the linearization of the buoyancy equation about a steady, horizontally uniform density stratification. To do so, they utilize a numerical model based on the linear balance equations (LBE), which are intermediate between QG and PE in both physical completeness and computational efficiency. The LBE solutions to the adiabaic, wind-driven ocean circulation problem are found to differ in many respects from the QG solutions. Most importantly, the LBE solutions have: less total transport; a broader, weaker gulf stream with sizable standing meanders and a shorter penetration scale into the interior; and a northward displacement of the western boundary current separation point. The essential source of these differences is found to be the more

accurate treatment of the Coriolis force in the LBE. Although McWilliams *et al.* are led to interpret the differences with the QG solutions as indications of significant improvement in the accuracy of the LBE solutions, no attempt was made to assess accuracy by comparison to comparable PE solutions.

To confirm that the higher order circulation features observed by McWilliams *et al.* in their LBE simulations are representative of the results for even more accurate systems of equations, such as the PE, we have duplicated one of their central experiments with the SPEM. The corresponding physical parameters for the rectangular, mid-latitude ocean basin are as follows: the domain dimensions are 3600 km × 2800 km × 5 km; the Coriolis parameter $f = f_0 + \beta y$, where $f_0 = 0.9 \times 10^{-4} s^{-1}$ and $\beta = 2 \times 10^{-11} m^{-1} s^{-1}$; and the initial level stratification is

$$N^2(z) = -\frac{g}{\rho_0} \frac{\partial \rho}{\partial z} = 5.9 \times 10^{-5} \exp(z/800m) s^{-2}. \tag{7.1}$$

The surface value $[N^2(0) = 5.9 \times 10^{-5} s^{-2}]$ has been chosen to reproduce the first baroclinic deformation radius (44.7 km) used by McWilliams *et al.*

In contrast to the test problems discussed in prior sections, the fluid is driven from above by an imposed, steady meridional wind stress, and is damped by both a linear bottom drag and a lateral viscosity of biharmonic form. In particular, recalling Eq. (2.13), (2.14), and (2.16), the forcing and damping terms in the u, v, and ρ equations are written

$$\mathscr{F}_u = -\left(\frac{2}{mn}\right)\left[\frac{\delta_{Nk} + \delta_{N-1,k}}{C_{\text{INT}}(O, N) + C_{\text{INT}}(O, N-1)}\right] * \tau_0 \cos\left[2\pi\left(y - \frac{1}{2}L_y\right)\Big/L_y\right],$$

$$D_u = -\left(\frac{2}{mn}\right)\left[\frac{\delta_{0k}}{C_{\text{INT}}(0, 0)}\right] * r_d u - \left(\frac{v_4 h}{mn}\right) \nabla^2 \nabla^2 u$$

$$\mathscr{F}_v = 0,$$

$$D_v = -\left(\frac{2}{mn}\right)\left[\frac{\delta_{0k}}{C_{\text{INT}}(0, 0)}\right] * r_d v - \left(\frac{v_4 h}{mn}\right) \nabla^2 \nabla^2 v,$$

$$\mathscr{F}_\rho = 0,$$

$$D_\rho = 0,$$

where

$$\tau_0 = 10^{-4} m^2 s^{-2},$$

$$r_d = 2.65 \times 10^{-4} ms^{-1},$$

$$v_4 = 8 \times 10^{10} m^4 s^{-1},$$

and

$$\nabla^2 = \left(\frac{mn}{h}\right)\left[\frac{\partial}{\partial\xi}\left(\frac{mh}{n}\right)\frac{\partial}{\partial\xi} + \frac{\partial}{\partial\eta}\left(\frac{nh}{m}\right)\frac{\partial}{\partial\eta}\right]$$

is the horizontal Laplacian operator. The lateral boundary conditions employed on the four side walls are the free-slip conditions:

$$(v_\xi - u_\eta) = 0$$

and

$$\nabla^2(v_\xi - u_\eta) = 0$$

on $\xi = 0$ and L_x, and $\eta = 0$ and L_y. Note that the surface wind stress and linearized bottom stress are treated as body forces on the uppermost and lowermost collocation levels, respectively. The biharmonic viscous terms are imposed at all collocation levels in the u and v equations. In contrast, the ρ equation contains no explicit forcing or damping.

Although the choice of Chebyshev polynomials as the vertical expansion functions is appropriate here, they are not optimal for this problem. That is because their turning points are distributed so as to favor equally the surface and bottom boundaries, whereas the solution is known to be surface intensified with little deep structure. Enhanced convergence and accuracy can therefore be obtained by utilizing a set of functions whose turning points are shifted so as to better resolve the surface currents. For the prescribed initial stratification (7.1), a good choice of expansion functions is a *stretched* set of Chebyshev polynomials $T_k(s(\sigma))$, where the monotonic stretching function

$$s(\sigma) = 2\left\{\frac{\exp[(z+5000)/1600]-1}{\exp[5000/1600]-1}\right\} - 1$$

$$= 2\left\{\frac{\exp[3.125(\sigma+1)/2]-1}{\exp[3.125]-1}\right\} - 1 \qquad (7.2)$$

is chosen such that $s(1) = 1$ and $s(-1) = -1$, and to produce a coordinate stretching near the surface proportional to $N(z)$. (This is the natural scale of variation for the stratification eigenfuntions of (7.1).) With $N = 4$, the location of the resulting shifted collocation points is then $z_k = [0, -216, -1030, -2761, -5000]$ m, corresponding to a nearly optimal distribution of the vertical collocation grid. For this choice of $s(\sigma)$, the vertical transformation matrices required by the model can be easily derived analytically in a manner similar to that shown in the Appendix. Note that, despite the realignment of the vertical collocation grid, the resulting expansion functions retain (and, in fact, exceed) the rapid convergence rate of the unstretched Chebyshev polynomials.

As is customary in such simulations, the wind stress is impulsively applied to the initially resting ocean at $t = 0$. In the results described below, a uniform horizontal grid spacing of 20 km, and a vertical representation of $N = 4$ stretched Chebyshev functions, were used. A time step of 20 min was found to be sufficient to guarantee stable integration.
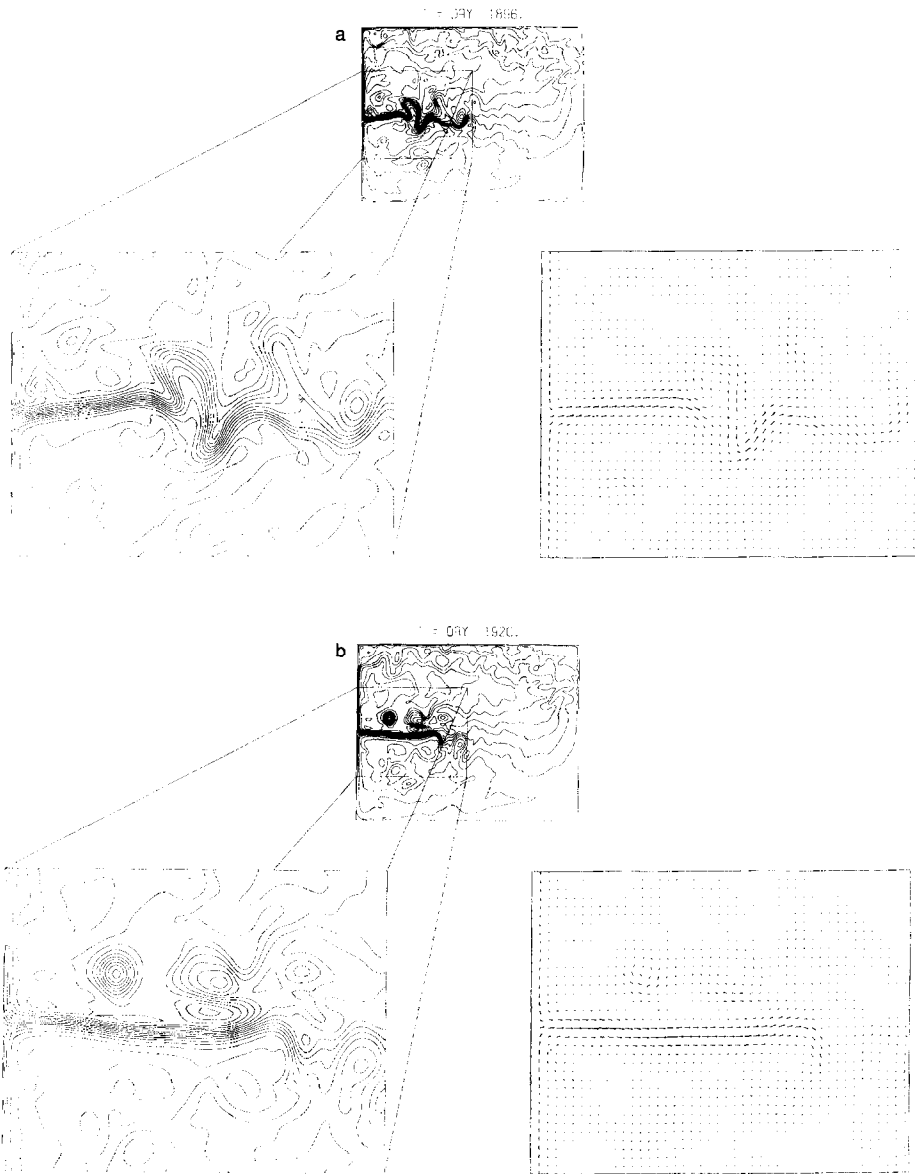
FIG. 9. Instantaneous circulation patterns from an eddy-resolving simulation of the wind-driven response of an adiabatic, mid-latitude ocean. Shown are maps of the contoured density field and horizontal velocity vectors at the first subsurface collocation level $(z = -216 \text{ m})$ in the region of the separated gulf stream $(0 \leqslant \xi \leqslant \frac{1}{2}L_x, \ \frac{1}{4}L_y \leqslant \eta \leqslant \frac{3}{4}L_y)$. Two sets of maps are shown, corresponding to: (a) day 1896, and (b) day 1920. The maximum velocity vector lengths plotted are 191 cm/s (day 1896) and 184 cm/s (day 1920). The density contour interval used is 0.08. Note the formation of an energetic, surface-intensified, warm core ring in this time interval.
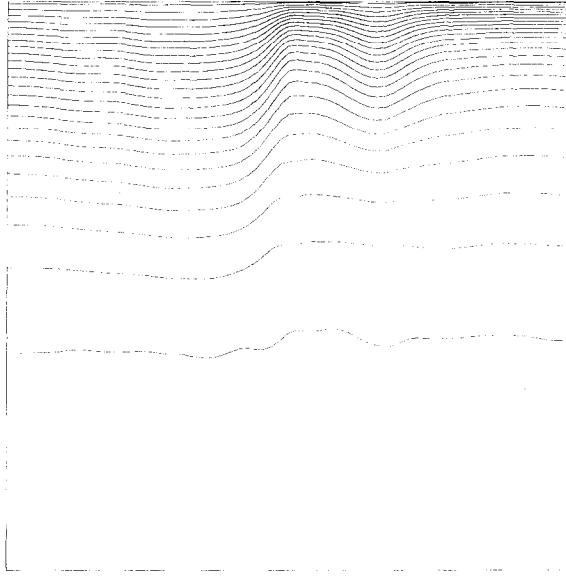
FIG. 10.   Meridional $(\eta - \sigma)$ cross section of the density field at day 1920 and $\zeta = 500$ km, showing the strong density front associated with the separated gulf stream. Note also the surface-intensified thermal structure of the warm core ring lying just to the north of the gulf stream.

After 5 years of integration, a time-dependent turbulent equilibrium has been reached in the basin. Figures 9 and 10 show a representative set of instantaneous pictures of the resulting circulation pattern at the first sub-surface collocation level $(z = -216 \text{ m})$. The near-surface horizontal velocity field (Fig. 9) is quite strong, reaching maximum speeds of $O(2 \text{ ms}^{-1})$. The vigorous separated current is in nearly geostrophic balance with a sharp, surface-intensified horizontal density front. Internal dynamical instabilities of the separated current produce energetic detached rings and eddies (e.g., Fig. 9b), whose non-linear interactions with the mean flow are substantial. Vertical sections through the boundary current (Fig. 10) emphasize the strong frontal nature of the circulation, and give a posteriori justification for the use of the stretching function (7.2) to better resolve the surface region.

With sufficient time averaging, the associated mean circulation and its statistics can be determined. Of particular interest in this simulation is the extent to which the primitive equation model confirms the qualitative discrepancies observed between the QG and LBE solutions to the adiabatic, wind-driven problem. The qualitative differences observed by McWilliams *et al.* are most easily visualized and appreciated by plotting the two-dimensional streamfunction field corresponding to the time-mean, non-divergent horizontal velocity at the surface. The three resulting figures for QG, LBE, and PE models are shown in Fig. 11. Both of the non-QG models have similar time-mean circulation patterns. In particular, both the LBE and PE solutions are asymmetric about the mid-latitude line $(y = \frac{1}{2}L_y)$ in contrast
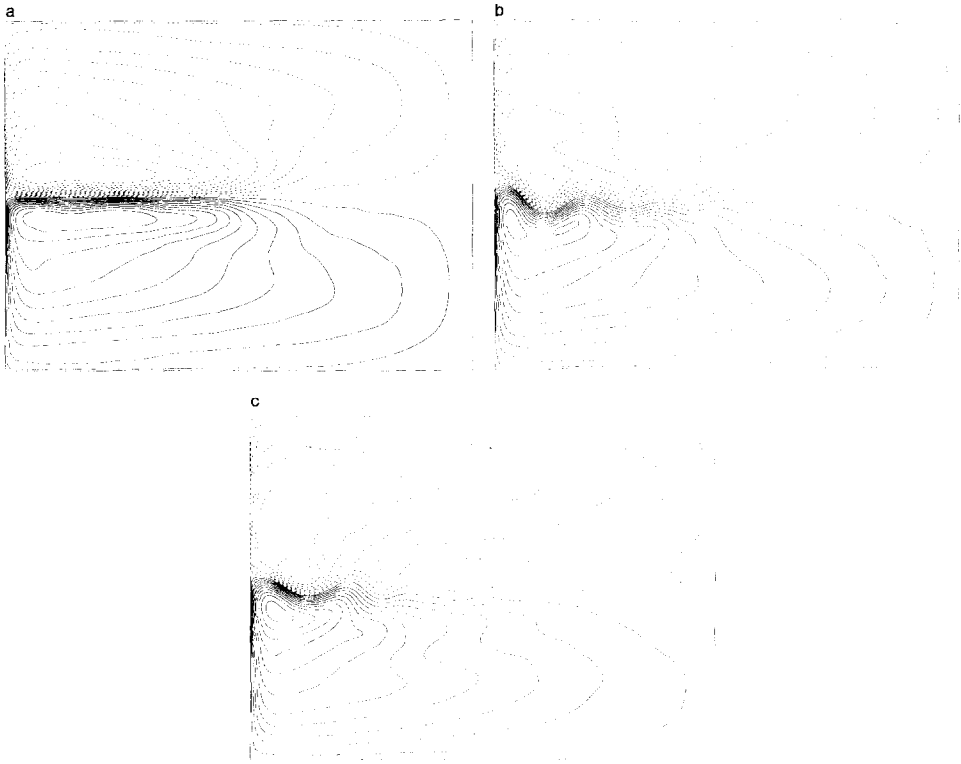
FIG. 11. Contour plots of the streamfunction field corresponding to the time-mean, non-divergent, surface layer velocity: (a) QG model; (b) LBE model; (c) PE model. The contour level is 0.125 (non-dimensional units) in all cases.

to the QG result. Both are characterized by a reduced strength of the separated gulf stream, and by substantially reduced penetration of the boundary current into the interior. Higher-order statistical properties of the time-dependent flow—for example, time-mean eddy kinetic energy—exhibit similar qualitative differences between the QG simulation, on the one hand, and the PE and LBE models, on the other. Results such as these underscore the sensitivity of numerical ocean circulation model behavior to the physical assumptions made, and emphasize the need for continued development of efficient, dynamically complete ocean models.

8. SUMMARY AND CONCLUDING REMARKS

We have described a new diabatic, rigid lid, hydrostatic, primitive equation model, designed for application to regional and basin-scale ocean circulation problems. Its unique advantage, we feel, lies in its simultaneous utilization of boundary-following coordinates and higher-order spectral approximation methods.

As demonstrated by the test problems described in Sections 4–7, the model is applicable to a wide range of oceanic processes and phenomena. In addition to the model description provided herein, a complete set of user documentation is also available [21].

A typical worry when implementing spectral methods, especially by "slow transform" methods, is that they will lead to a computationally inefficient code. This prospect is particularly worrisome here, where vertical operations are carried out by matrix multiplication and where the number of vertical collocation points is typically small ($O(10)$). (On supercomputers, such as the Cray X-MP, efficient operation is closely tied to the degree of vectorization, and to the use of long vector lengths.) Fortunately, due to the "regularization" of the computational domain which results from the simultaneous use of sigma and horizontal orthogonal curvilinear coordinates, the spectral operations required by the model are highly vectorizable. For example, consider a case where there are a total of (say) $L \times M$ horizontal gridpoints, at each of which a vertical operation such as integration is needed. The requisite $L \times M$ integrations can then be obtained entirely via manipulations of vectors of length $L \times M$. Since in most applications $L \times M$ will be many hundreds or thousands, and will typically be orders of magnitude greater than the number of vertical expansion functions (N), vectorization of vertical operations by horizontal gridpoint is extremely efficient.

As a result, in part, of this vectorization technique, the SPEM is of comparable efficiency to other operational primitive equation ocean circulation models, despite its utilization of the higher order spectral collocation method in the σ coordinate. For example, the basin-scale, wind-driven ocean circulation simulation described in Section 7 has been found to run at over 120 Mflops on a single processor of the Cray X-MP at the National Center for Atmospheric Research (NCAR). In terms of cpu time, this translates to approximately 1×10^{-5} cpu-s per grid point per time step. The well-known models of Cox and Bryan, and Gent and Cane, have comparable cpu requirements [8].

Lastly, it should be noted that further gains in accuracy and convergence properties could be made by simultaneous utilization of higher order (spectral, spectral-finite-element, or fourth-order finite-difference) methods in both the horizontal and vertical dimensions. Several such models are currently being formulated and tested. These developments—as well as parallel innovations in the areas of adaptive grids [37], spectral multi-grid techniques [7], and others—are likely to have a significant impact on ocean modeling in the decade of the 1990s.

APPENDIX: Chebyshev Polynomial Basis Functions

As described in Section 3a, the $P_k(\sigma)$ expansion functions used in the vertical spectral method can be chosen somewhat arbitrarily. Here we review the form of the matrix operators when the $P_k(\sigma)$ are a modified form of Chebyshev polynomials of the first kind [$T_k(\sigma)$; see, e.g., (1) and (18)]. The $T_k(\sigma)$ are defined over the

$$P_k(\sigma) = \begin{cases} T_0(\sigma), & k = 0 \\ T_k(\sigma), & k \leqslant 1, k \text{ odd} \\ T_k(\sigma) + \dfrac{1}{k^2 - 1}, & k \geqslant 2, k \text{ even,} \end{cases} \quad (A.1)$$

which conform to the required integral property that only $P_0(\sigma)$ have a non-zero vertical integral. The collocation points σ_n are located at the extrema of the highest order polynomial $P_N(\sigma)$; hence,

$$\sigma_n = \cos[\pi(n - N)/N], \qquad 0 \leqslant n \leqslant N. \quad (A.2)$$

Matrix F (see Eq. (3.3)) may now be evaluated from (A.1) and (A.2). Substituting (A.1) into (3.6) gives the elements of matrix R:

$$R_{nk} = \frac{\partial P_k}{\partial \sigma}(\sigma_n) = \frac{k \sin(k\theta_n)}{\sin \theta_n}, \quad (A.3)$$

where $\theta_n = \cos^{-1}(\sigma_n)$. Similarly, (A.1) and (3.8) give the elements of matrix $\mathscr{S}$:

$$\mathscr{S}_{nk} = \int_{\sigma_n}^{1} P_k(\sigma)\, d\sigma = \begin{cases} (1 - \sigma_n), & k = 0 \\ \frac{1}{2}(1 - \sigma_n^2), & k = 1 \\ \left[\dfrac{\cos(k+1)\sigma}{2(k+1)} - \dfrac{\cos(k-1)\sigma}{2(k-1)}\right]_{\cos^{-1}(\sigma_n)}^{0} & k > 1, \text{ odd} \\ \left[\dfrac{\cos(k+1)\sigma}{2(k+1)} - \dfrac{\cos(k-1)\sigma}{2(k-1)}\right]_{\cos^{-1}(\sigma_n)}^{0} & \\ \quad + (1 - \sigma_n)\dfrac{1}{k^2 - 1} & k > 1, \text{ even.} \end{cases} \quad (A.4)$$

Finally, the differentiating and integrating operators C_{DZ} and C_{INT} are computed by first inverting F and calculating the products $C_{DZ} = RF^{-1}$ and $C_{INT} = \mathscr{S}F^{-1}$.

REFERENCES

1. M. ABRAMOWITZ ANBD I. A. STEGUN, *Handbook of Mathematical Functions*, Appl. Math. Ser., No. 55 (Nat. Bur. of Standards, Washington, DC, 1972).
2. J. S. ALLEN, J. A. BARTH, AND P. A. NEWBERGER, "On Intermediate Models for Barotropic Continental Shelf and Slope Flow Fields. Part I. Formulation and Comparison of Exact Solutions," in press.
3. A. ARAKAWA AND V. R. LAMB, "Computational Design of the Basic Dynamical Processes of the UCLA General Circulation Model," in *Methods of Computational Physics*, Vol. 17 (Academic Press, New York, 1977), p. 174.
4. A. F. BLUMBERG AND G. L. MELLOR, "A Description of a Three-Dimensional Coastal Ocean Circulation Model," in *Three-Dimensional Coastal Ocean Models*, edited by N. Heaps (American Geophysical Union, Washington, DC, 1987), p. 1.
5. K. H. BRINK, *J. Phys. Oceanogr.* **16**, 2150 (1986).
6. K. H. BRINK, *Rev. Geophys.* **25**, 204 (1987).
7. D. BROUTMAN AND R. GRIMSHAW, "Spectral Multigrid and Collocation Methods for Barotropic Nondivergent Flow over Irregular Coastal Topography," in press.
8. F. BRYAN AND P. GENT, National Center for Atmospheric Research, Boulder, CO, private communications (1989).
9. V. T. BUCHWALD AND J. K. ADAMS, *Proc. Roy. Soc. A* **305**, 235 (1968).
10. D. C. CHAPMAN, *J. Phys. Oceanogr.* **15**, 1060 (1985).
11. M. D. COX, *J. Phys. Oceanogr.* **15**, 1312 (1985).
12. A. M. DAVIES, "Spectral Models in Continental Shelf Sea Oceanography," in *Three-Dimensional Coastal Ocean Models*, edited by N. Heaps (American Geophysical Union, Washington, DC, 1987), p. 71.
13. J. C. EVANS, D. B. HAIDVOGEL, AND W. R. HOLLAND, *Rev. Geophys.* **25**, 235 (1987).
14. G. R. FLIERL, *Dyn. Atmos. Oceans* **2**, 341 (1978).
15. N. G. FREEMAN, A. M. HALE, AND M. B. DANARD, *J. Geophys. Res.* **77**, 1050 (1972).
16. P. R. GENT AND M. A. CANE, *J. Comput. Phys.* **81**, 444 (1989).
17. D. B. HAIDVOGEL AND K. H. BRINK, *J. Phys. Oceanogr.* **6**, 2159 (1986).
18. D. B. HAIDVOGEL AND T. ZANG, *J. Comput. Phys.* **30**, 167 (1979).
19. G. J. HALTINER AND R. T. WILLIAMS, *Numerical Prediction and Dynamic Meteorology*, 2nd ed. (Wiley, New York, 1980), p. 111.
20. N. S. HEAPS (Ed.), *Three-Dimensional Coastal Ocean Models* (American Geophysical Union, Washington, DC, 1987).
21. K. S. HEDSTROM, "User's Manual for a Semi-Spectral Primitive Equation Ocean Circulation Model," Institute for Naval Oceanography, Stennis Space Center, MS, 1990.
22. W. R. HOLLAND, *J. Phys. Oceanogr.* **8**, 363 (1978).
23. J. M. HUTHNANCE, *J. Phys. Oceanogr.* **8**, 74 (1978).
24. D. C. IVES AND R. M. ZACHARIAS, "Conformal mapping and orthogonal grid generation," Paper No. 87-2057, AIAA/SAE/ASME/ASEE 23rd Joint Propulsion Conference, San Diego, California, June 1987 (unpublished).
25. E. N. LORENZ, *Tellus* **12**, 364 (1960).
26. J. C. WILLIAMS, N. J. NORTON, P. R. GENT, AND D. B. HAIDVOGEL, "A Linear Balanced Model of Wind-Driven, Mid-Latitude Ocean Circulation," *J. Phys. Oceanog.* **20**, 1349 (1990).
27. R. N. MILLER, A. R. ROBINSON, AND D. B. HAIDVOGEL, *J. Comput. Phys.* **50**, 38 (1983).
28. W. H. MUNK, *J. Meteorol.* **7**, 79 (1950).
29. J. C. J. NIHOUL AND B. M. JAMART (Eds.), *Three-Dimensional Models of Marine and Estuarine Dynamics* (Elsevier, New York, 1987).
30. J. J. O'BRIEN (Ed.), Advanced Physical Oceanographic Modelling (Reidel, Boston, 1986).
31. I. ORLANSKI, *J. Comput. Phys.* **21**, 251 (1976).
32. S. A. ORSZAG AND M. ISRAELI, *Ann. Rev. Fluid Mech.* **6**, 281 (1974).

33. N. A. PHILLIPS, *J. Meteorol.* **14**, 184 (1957).
34. A. R. ROBINSON, M. A. SPALL, L. J. WALSTAD, AND W. G. LESLIE, *Dyn. Atmos. Oceans* **13**, 301 (1989).
35. W. J. SCHMITZ AND W. R. HOLLAND, *J. Geophys. Res.* **91**, 9624 (1986).
36. A. J. SEMTNER AND R. M. CHERVIN, *J. Geophys. Res.* **93**, 15, 502 (1988).
37. W. SKAMAROCK, J. OLIGER, AND R. L. STREET, *J. Comput. Phys.* **80**, 27 (1989).
38. H. STOMMEL, *Trans. Amer. Geophys. Union* **99**, 202 (1948).
39. J. L. WILKIN AND D. C. CHAPMAN, *J. Phys. Oceanogr.* **17**, 713 (1987).
40. J. L. WILKIN AND D. C. CHAPMAN, *J. Phys. Oceanogr.* **20**, 396 (1990).